

High-resolution and non-oscillatory solution of the St. Venant equations in non-rectangular and non-prismatic channels

Solution d'ordre élevé et non oscillante des équations de Saint-Venant dans les canaux ni rectangulaires ni prismatiques

BRETT F. SANDERS, *M. IAHR, Department of Civil and Environmental Engineering, University of California, Irvine, CA 92697*

ABSTRACT

A scheme to model open channel flow over wet and dry beds in non-rectangular and non-prismatic channels is presented. The scheme is second-order accurate, stable for Courant numbers up to unity, and monotonicity preserving. The scheme solves the St. Venant equations using a Godunov-type finite volume method. Mass and momentum fluxes are computed using a Roe-type Riemann solver, the MUSCL (Monotone Upwind Scheme for Conservation Laws) approach is applied for second-order spatial accuracy, and a treatment is introduced to model the hydrostatic pressure force exerted by the channel walls in the stream wise direction. The treatment permits momentum fluxes and the channel wall force to be balanced to numerical precision, preventing the artificial acceleration of the flow. Comparisons between model results, exact solutions, and experimental data show that the scheme is robust. Accurate and monotone results are obtained in the presence of discontinuities, supercritical flow, subcritical flow, transcritical flow, and dry-bed flow problems without the need for special front-tracking approaches or deforming grids. In addition, the scheme will conserve mass to numerical precision in all applications.

RÉSUMÉ

Un schéma est présenté pour modéliser les écoulements à surface libre sur des fonds secs ou mouillés, dans les canaux qui ne sont ni rectangulaires ni prismatiques. Le schéma est précis au second ordre, stable pour les nombres de Courant inférieurs à l'unité, et préserve la monotonie. Le schéma résout les équations de Saint-Venant avec une méthode de volumes finis de type Godunov. Les flux de masse et de quantité de mouvement sont calculés avec un solveur de Riemann de type Roe, l'approche MUSCL (schéma amont monotone pour les lois de conservation) est appliqué pour la précision spatiale au second ordre, et un traitement est introduit pour modéliser la force de pression hydrostatique exercée par les parois du canal dans la direction du courant. Ce traitement permet d'équilibrer, à la précision numérique près, les flux de quantité de mouvement et l'effort exercé par les parois, ce qui évite une accélération artificielle de l'écoulement. Les comparaisons faites entre résultats du modèle, solutions exactes et données expérimentales, montrent que le schéma est robuste. Des résultats précis et monotones sont obtenus en présence de discontinuités, d'écoulements supercritique, sous-critique, et trans-critique, et de problèmes d'écoulement sur fond sec, sans faire appel à des approches spéciales de suivi de front ou de grilles déformables. De plus, le schéma conservera la masse, à la précision numérique près, dans toutes les applications.

Introduction

Non-oscillatory finite volume schemes for the shallow-water equations in both one and two spatial dimensions have been the subject of much research (Glaister 1988, Alcrudo et al. 1992, Alcrudo and Garcia-Navarro 1993, Zhao et al. 1994, Nujić 1995, Mingham and Causon 1998). Progress has been made using Godunov-type finite volume schemes that utilize Riemann solvers to evaluate fluxes at cell interfaces and the MUSCL (Monotone Upwind Scheme for Conservation Laws) method for second-order spatial accuracy (Hirsch 1990).

The advantages of Godunov-type finite volume schemes are numerous. First, the schemes permit a high-resolution and monotone numerical solution to a wide variety of flows including subcritical, supercritical, transcritical, and dry bed flow problems. Second, the schemes are highly flexible in multiple dimensions, in that a wide variety of irregular solution domains can be discretized using either structured or unstructured grids. Third, the schemes are generally implemented using explicit time-marching algorithms and are stable for Courant numbers less than unity. As a result, the need to solve computationally expensive matrix problems at each time step, which exists when applying the finite element method (e.g. Katopodes 1984), is avoided and

a rapid solution of the most complicated problems becomes possible on desktop computers. Fourth, a wide range of boundary conditions, including open boundaries, can be easily implemented. Fifth, mass can be conserved to numerical precision, generally $O(10^{-14})$ on desktop computers.

However, one-dimensional solution schemes with the properties described above have been slow to develop for non-rectangular and non-prismatic channels--precisely the configurations that are commonly encountered in engineering practice. A Godunov-type scheme for flow in rectangular, prismatic channels was first considered by Glaister (1988), and non-rectangular prismatic channel flow has been considered by Alcrudo et al. (1992), but further advances have not been forthcoming. Two aspects of the one-dimensional formulation make a Godunov finite-volume formulation difficult in non-rectangular and non-prismatic channels. First, non-rectangular channels possess a spectrum of wave speeds across the channel width. As a result, wave dispersion occurs, and a well-posed Riemann problem cannot be formulated. Second, the integral form of the momentum conservation equation contains a pressure term, in the case of non-prismatic channels, that accounts for the force in the stream wise direction exerted by the channel walls (Cunge et al. 1980). Unless this term is resolved with a numerical accuracy equivalent to that of the inertial and

Revision received February 16, 2000. Open for discussion till December 31, 2001.

pressure fluxes in the momentum equation, the benefit of highly resolved momentum fluxes provided by the Riemann solver will be lost and the scheme will artificially accelerate the flow.

In this paper, a Godunov-type finite volume scheme is presented to address these aforementioned problems and to subsequently achieve a non-oscillatory and second-order accurate solution of the St. Venant equations. By comparing model results to exact solutions and experimental data, the scheme is shown to remain stable and achieve accurate results in the presence of discontinuities, subcritical flow, supercritical flow, transcritical flow, dry-bed problems, and problems of variable channel cross-section.

One-dimensional flow equations

One-dimensional equations describing unsteady channel flow are based upon the assumptions that: (a) the velocity is uniform over the channel cross section, (b) vertical accelerations are negligible, (c) boundary friction and turbulence can be modeled by resistance laws such as the Manning/Strickler formula, and (d) the slope of the channel is small, such that the cosine of the angle between the plane of the channel bottom and the horizontal plane is essentially unity. The integral form of the continuity and momentum equations is given by Cunge et al. (1980) and appear, respectively, as follows,

$$\int_{x_1}^{x_2} [A_{t_2} - A_{t_1}] dx + \int_{t_1}^{t_2} [(AV)_{x_2} - (AV)_{x_1}] dt = 0 \quad (1)$$

$$\begin{aligned} & \int_{x_1}^{x_2} [(AV)_{t_2} - (AV)_{t_1}] dx \\ & + \int_{t_1}^{t_2} \left[(V^2 A + gA\bar{y})_{x_2} - (V^2 A + gA\bar{y})_{x_1} \right] dt \\ & = \int_{t_1}^{t_2} \int_{x_1}^{x_2} F_c dx dt + \int_{t_1}^{t_2} \int_{x_1}^{x_2} gA(S_o - S_f) dx dt \end{aligned} \quad (2)$$

where A is the cross-sectional area, V is the cross-sectionally averaged velocity, \bar{y} is the depth from the free surface to the centroid of the wetted channel cross-section, F_c represents the component of the hydrostatic force in the x -direction exerted by the channel walls, S_o is the channel slope, S_f is the friction slope, usually given by the Manning/Strickler or Chézy formula, x_1 and x_2 define the spatial domain, and t_1 and t_2 define the temporal domain.

Eqs. (1) and (2) can be applied in any case where the flow satisfies conditions (a)-(d) above. It is more common to instead solve a differential form of the flow equations, but all differential forms cannot necessarily be applied to any flow satisfying (a)-(d). For example, the divergent form of the equations is given by,

$$\frac{\partial A}{\partial t} + \frac{\partial (AV)}{\partial x} = 0 \quad (3)$$

$$\frac{\partial (AV)}{\partial t} + \frac{\partial}{\partial x} (V^2 A + gA\bar{y}) = F_c + gA(S_o - S_f) \quad (4)$$

while the form most commonly used in engineering practice is given by,

$$\frac{\partial h}{\partial t} + \frac{1}{T} \frac{\partial Q}{\partial x} = 0 \quad (5)$$

$$\frac{\partial Q}{\partial t} + \frac{\partial}{\partial x} \left(\frac{Q^2}{A} \right) + gA \frac{\partial h}{\partial x} = gA(S_o - S_f) \quad (6)$$

where $Q=VA$, h is the depth of flow, and T is the width of the channel cross-section at the free surface level.

Both the divergent form given by Eqs. (3) and (4) and the form given by Eqs. (5) and (6) are applicable to non-prismatic channels. However, Eqs. (3) and (4) can be integrated over the computational cell and applied in the presence of discontinuities, such as those arising from surges and shocks. In contrast, Eqs. (5) and (6) cannot be integrated over the cell and applied in the presence of discontinuities and will not conserve mass to numerical precision when discretized, so these are not utilized here.

When solving Eqs. (3) and (4) by the finite volume method, the central challenge is presented by the computation of momentum fluxes and pressure force F_c . These forces must be resolved with an identical precision. Otherwise, the scheme will artificially accelerate the flow. In the next section, a computational approach based on the finite volume method is outlined for precisely and accurately solving Eqs. (3) and (4).

Numerical solution by finite volume method

Using the finite volume method (FVM), the spatial domain is discretized into N computational cells of length Ω . The dependent variables are defined at the cell centers and represent the average value within each cell. Fluxes, on the other hand, are evaluated at the interfaces between cells. Depth-area relationships, $A=A(h)$, are also defined at the cell interfaces, and linear averaging of channel properties is performed to obtain depth-area relationships at cell centers. Hence, channel dimensions such as bottom width and side slope are assumed to vary linearly along the cell length in the case of non-prismatic channels.

It is useful to work with the equations in matrix form, so the spatial integral of Eqs. (3) and (4) over one cell of length, Ω , is written as,

$$\frac{\partial}{\partial t} \int_{\Omega} \mathbf{U} d\Omega + \int_{\Omega} \frac{\partial \mathbf{F}}{\partial x} d\Omega = \int_{\Omega} \mathbf{S} d\Omega \quad (7)$$

where the conservative variables, fluxes, and source terms are given, respectively, by

$$\mathbf{U} = \begin{pmatrix} A \\ VA \end{pmatrix} \quad \mathbf{F} = \begin{pmatrix} VA \\ V^2 A + gA\bar{y} \end{pmatrix} \quad \text{and} \quad \mathbf{S} = \begin{pmatrix} 0 \\ F_c + gA(S_o - S_f) \end{pmatrix} \quad (8)$$

Recalling that the conservative variables are defined to be the cell average, and applying Green's theorem, Eqs. (7) become,

$$U^{k+1} = U^k - \frac{\Delta t}{\Omega} (F_R - F_L) + \Delta t S \quad (9)$$

where the subscripts R and L appearing on the flux vector refer to the fluxes at the right and left boundary of each cell, respectively; and the superscripts $k+1$ and k reflect the $t+\Delta t$ and t time levels, respectively. If the flux and source terms are defined to be the average over the time step, then Eqs. (9) is an exact statement of mass conservation and momentum balance that is equivalent to the integral relations given by Eqs. (1) and (2). Consequently, the update equation given by Eqs. (9) is the basis of the finite volume method.

A predictor-corrector scheme known as Hancock's method is applied here for time-integration (van Albada et al. 1982). In the predictor step, the cell-average solution is advanced to the half-time level. Fluxes are then evaluated at the half-time level and at the interface between cells. The corrector step then advances the cell-average solution from the base time level to the next full time level using fluxes evaluated at the half-time level. Second order spatial accuracy is obtained by employing the MUSCL approach which constructs a piecewise linear distribution of the solution at the half-time level (Hirsch 1990). Hancock's method has previously been utilized by Bradford and Katopodes (1999), and Sanders and Bradford (2001) with much success, and its structure leads to an algorithm that is logical, modular, and easy to program. A chief advantage of this approach is that the interface fluxes are computed with second-order accuracy. Hence, there is no need to compute second-order corrections, as is done in other finite volume schemes, e.g., Alcrudo et al. (1982).

Predictor Step

The predictor step estimates the solution at the half-time level by solving the primitive form of the flow equations given by,

$$\frac{\partial A}{\partial t} + V \frac{\partial A}{\partial x} + A \frac{\partial V}{\partial x} = 0 \quad (10)$$

$$\frac{\partial V}{\partial t} + g \frac{\partial h}{\partial x} + V \frac{\partial V}{\partial x} = g (S_o - S_f) \quad (11)$$

which follow from Eqs. (3) and (4). The primitive form of the flow equations is solved for simplicity and computational efficiency. Note that the 'momentum' equation given by Eq. (11) does not explicitly treat the hydrostatic force F_c . Rather, this force is imbedded within the term $g \frac{\partial h}{\partial x}$ in Eq. (11), as is described by Cunge et al. (1980). Indeed, both Eq. (6) and Eq. (11) are termed 'dynamic' equations, not momentum balance equations. The half-time solution in the j^{th} cell is therefore computed as follows,

$$A_j^{k+1/2} = A_j^k - \frac{\Delta t}{2\Omega} (V \overline{\Delta A} + A \overline{\Delta V})_j^k \quad (12)$$

$$V_j^{k+1/2} = V_j^k - \frac{\Delta t}{2\Omega} (g \overline{\Delta h} + V \overline{\Delta V})_j^k + \frac{g \Delta t}{2} \left((S_o)_j^k - \frac{1}{2} (S_f)_j^k - \frac{1}{2} (S_f)_j^{k+1/2} \right) \quad (13)$$

where the overbar indicates that the cell gradients are *limited*. The use of limited gradients in Eqs. (12) and (13) prevents the over- and under-shoots common to second-order schemes. The limited gradient of depth and velocity in cell j is given by,

$$\begin{aligned} \overline{\Delta h}_j &= \text{avg} (h_{j+1} - h_j, h_j - h_{j-1}) \\ \text{and} \\ \overline{\Delta V}_j &= \text{avg} (V_{j+1} - V_j, V_j - V_{j-1}) \end{aligned} \quad (14)$$

The choice of the averaging function, $\text{avg}(\alpha, \beta)$, is important. Nonlinear averages termed flux or slope limiters should be applied (Sweby 1984). Here, the Superbee limiter is used. It is given as (Hirsch 1990),

$$\text{avg}(\alpha, \beta) = \begin{cases} \min \text{mod}(\max \text{mod}(\alpha, \beta), \min \text{mod}(2\alpha, 2\beta)), & \alpha\beta > 0 \\ 0 & \alpha\beta < 0 \end{cases} \quad (15)$$

where $\min \text{mod}$ and $\max \text{mod}$ return the argument with the smallest and largest modulus, respectively. Though not utilized here, an alternative approach to computing the limited depth involving the free surface elevation should be considered when the bed elevation is highly variable, as is shown by Nujić (1995).

Since cross-sectional area is a function of depth, the gradient of the cross-sectional area is computed as,

$$\overline{\Delta A}_j = \frac{A_{j+1} (h_j + \overline{\Delta h}_j) - A_{j-1} (h_j - \overline{\Delta h}_j)}{2} \quad (16)$$

Hence, the depth is extrapolated to neighboring cell centers where the associated cross-sectional areas are computed. The difference in cross-sectional area then gives the gradient.

Note that this scheme requires the depth to be defined at cell centers in addition to the cross-sectional area. Since area and depth are functionally related through the cross-sectional properties of the channel, one can be computed from the other. However, iterative procedures may be required to compute h from A in natural channels where the depth-area relationship is complex. On the other hand, the depth-area relationship is linear in h for rectangular channels and quadratic in h for trapezoidal channels, so the depth can be computed explicitly from A in many applications. The source terms appearing on the right hand side of Eq. (13) are evaluated as follows,

$$(S_o)_j = -\frac{z_{j+1/2} - z_{j-1/2}}{\Omega} \quad \text{and} \quad (S_f)_j = \frac{n^2 V_j |V_j|}{(R_h)_j^{2/3}} \quad (17)$$

where z is the elevation of the bed (defined at cell faces), n is the Manning coefficient, and R_h is the hydraulic radius. Note that the resistance term, S_f is discretized implicitly in Eq. (13) using the trapezoidal rule. This treatment is necessary when computing wave propagation over a dry bed, as it allows for a stable integration using Courant numbers up to unity in spite of the large friction slope present at the wet/dry interface. The additional computational cost per time step associated with this semi-implicit approach, compared with an explicit approach, is minimal because Eq. (13) represents a quadratic expression for $V_j^{k+1/2}$ that can easily be solved by the well-known quadratic formula. Hence, the semi-implicit approach reduces the overall computational cost for dry bed problems compared with an explicit approach because relatively larger time steps can be taken.

MUSCL Extrapolation

Once the predictor step has computed the cell-average solution at the half-time level, MUSCL variable extrapolation is employed to construct the solution at the left and right sides of each cell face (van Leer 1979). At the $j+1/2$ cell boundary, the variables h and V on the left and right face of the boundary are given as,

$$h_L = h_j + \frac{1}{2}(\overline{\Delta h_j}) \quad h_R = h_{j+1} - \frac{1}{2}(\overline{\Delta h_{j+1}}) \quad (18)$$

$$V_L = V_j + \frac{1}{2}(\overline{\Delta V_j}) \quad V_R = V_{j+1} - \frac{1}{2}(\overline{\Delta V_{j+1}}) \quad (19)$$

The area A on the left and right side of each cell face is then computed using the extrapolated depths and the depth-area relationship defined at the cell face. Hence,

$$A_L = A(h_L) \quad \text{and} \quad A_R = A(h_R) \quad (20)$$

It is possible to extrapolate A from the cell center to the cell face, but this is undesirable for two reasons. First, depth-area relationships are defined at the cell face, so A_R and A_L should reference identical cross-sectional properties, not average properties from neighboring cells. Second, A is not distributed linearly across the cell in non-rectangular channels if h is distributed linearly, so linear extrapolation is not warranted.

Flux Computation

A numerical flux function is applied to compute the mass and momentum fluxes following MUSCL extrapolation to each cell interface. In the case of a rectangular channel, two states separated by an interface constitute a Riemann problem that can be solved to evaluate the desired mass and momentum fluxes. However, in non-rectangular channels, Riemann invariants cannot be formulated except for the special case of a triangular channel. That is, the well-known Riemann invariants of shallow-water hydraulics, $R^+ = V + 2a$ and $R^- = V - 2a$ are only valid for rectangular channels (Chaudhry 1993). In the case of a triangular channel, it can be shown that $R^+ = V + 4a$ and $R^- = V - 4a$. Neverthe-

less, the Riemann-type problem that is formulated here for non-rectangular channels is not well posed in the sense that an exact solution cannot be obtained for arbitrary channel cross-sections. While the outlook for FVM in one-dimensional hydraulics may now appear to be bleak, the reality is actually the opposite. This is because Riemann problems are rarely solved exactly to evaluate interface fluxes, for the accuracy gained by solving the nonlinear Rankine-Hugoniot relations is lost through the process of cell averaging that occurs with each time step. The common practice is to instead solve a locally linearized Riemann problem, and this can be accomplished using a variety of numerical flux-functions. Here, Roe's scheme is used.

Roe's numerical flux function, originally developed for solutions of the Euler equations of compressible gas dynamics, has been applied in numerous one- and two-dimensional shallow-water algorithms (e.g. Glaister 1988, Alcrudo et al. 1992, Zhao et al. 1994, Nujic 1995). It provides the interface flux as follows (Roe 1981),

$$F_I = \frac{1}{2} (F_L + F_R - |\hat{A}_U| \Delta U) \quad (21)$$

where A_U is the Jacobian matrix given by dF/dU , and the matrix $|\hat{A}_U|$ is defined as,

$$|\hat{A}_U| = \hat{R} |\hat{\Lambda}| \hat{L} \quad (22)$$

where $|\hat{\Lambda}|$ is the diagonal matrix containing the absolute values of all the eigenvalues of \hat{A}_U , and \hat{R} and \hat{L} represent the matrices of right and left eigenvectors, respectively. For one-dimensional flow, these matrices are given as,

$$\hat{\Lambda} = \begin{pmatrix} \hat{V} - \hat{a} & 0 \\ 0 & \hat{V} + \hat{a} \end{pmatrix} \quad \hat{R} = \begin{pmatrix} 1 & 1 \\ \hat{V} - \hat{a} & \hat{V} + \hat{a} \end{pmatrix} \quad (23)$$

$$\text{and} \quad \hat{L} = \frac{1}{2\hat{a}} \begin{pmatrix} \hat{V} + \hat{a} & -1 \\ -\hat{V} + \hat{a} & 1 \end{pmatrix}$$

where $a = (gAT)^{1/2}$. The quantities denoted with a hat are known as Roe averages. Roe averages represent nonlinear estimates of the variables V and a at the cell face, computed locally, that enforce several conditions including the following (Roe 1981),

$$F_R - F_L \equiv \hat{A}_U (U_R - U_L) \quad (24)$$

as has been shown by Alcrudo et al. (1992). The Roe average of velocity is given by,

$$\hat{V} = \frac{\sqrt{A_L} V_L + \sqrt{A_R} V_R}{\sqrt{A_L} + \sqrt{A_R}} \quad (25)$$

To enforce Eq. (24), \hat{a} must satisfy,

$$gA_R \bar{y}_R - gA_L \bar{y}_L = \hat{a}^2 (A_R - A_L) \quad (26)$$

For the case of a trapezoidal cross section with the properties,

$$A = bh + mh^2 \quad \text{and} \quad \bar{y} = \frac{bh^2/2 + mh^3/3}{bh + mh^2} \quad (27)$$

where $b = b(x)$ is the channel width at the bottom, and $m = m(x)$ is the inverse slope of the channel walls, the Roe average of the wave speed is given by,

$$\hat{a} = \sqrt{\frac{g(2mh_L^2 + 3bh_L + 2mh_L h_R + 3bh_R + 2mh_R^2)}{6(mh_L + b + mh_R)}} \quad (28)$$

where h_L and h_R are the depths on the left and right side of the cell face, respectively. For those channel cross-sections of a natural geometry, the wave speed at the cell interface can be selected as (Alcrudo et al. 1992)

$$\hat{a} = \begin{cases} \sqrt{(gA_R \bar{y}_R - gA_L \bar{y}_L)/(A_R - A_L)}, & A_R \neq A_L \\ a_L = a_R, & A_R = A_L \end{cases} \quad (29)$$

However, Eq. (29) should be employed cautiously as floating point errors can develop when $A_L \approx A_R$.

Roe's method will compute a jump within a depression wave when the flow is critical. To correct this problem, a local depression wave is introduced at critical flow locations by replacing the eigenvalues $|\lambda| = |V \pm a|$ in Eq. (22) with the following,

$$|\hat{\lambda}|^* = \frac{\hat{\lambda}^2}{\Delta\lambda} + \frac{\Delta\lambda}{4} \quad (30)$$

when $|\lambda| < \Delta\lambda/2$. Van Leer et al. (1989) has shown that $\Delta\lambda = 4(\lambda_R - \lambda_L)$ yields the appropriate amount of dissipation when marching to a steady-state.

To improve computational efficiency, a simplified version of Roe's solver can be used in place of Eq. (21) (Nujic 1995). The simplified flux function is given by,

$$F_i = \frac{1}{2}(F_L + F_R - \alpha \Delta U) \quad (31)$$

where α is a parameter that can be computed locally or globally. Here, it is selected locally as,

$$\alpha = \max(|V + a|, |V - a|) \quad (32)$$

This approach is useful in conjunction with the MUSCL reconstruction because ΔU across the cell interface is small. However, a small reduction in accuracy can still be expected. In addition, Eqs. (31) should not be used in the context of a first-order accurate scheme where ΔU is considerably larger.

Computation of F_c

The benefits associated with the Riemann problem solution and the MUSCL reconstruction will be of little use unless a similarly accurate treatment of the force F_c is obtained. The precise computation of this force is essential in non-prismatic channels. Recall that this term represents the hydrostatic pressure force in the direction of the channel centerline that is exerted by the channel walls as a result of an increase in channel width and under conditions where the depth is constant and given by the average depth in the cell. Using Hancock's scheme, the cell average value of area and depth are defined at the cell centers, so the average depth at the half-time level, $h_j^{k+1/2}$, is known. The pressure force, F_c , can therefore be precisely evaluated as follows,

$$F_c = g \bar{y}' \Delta A \quad (33)$$

where

$$\Delta A = A_{j+1/2}(h_j) - A_{j-1/2}(h_j) \quad (34)$$

and $A_{j+1/2}(h_j)$ and $A_{j-1/2}(h_j)$ represent the cross sectional areas evaluated using the depth at the cell center and the depth-area relationship at the right and left face of the j^{th} cell, respectively. In addition, \bar{y}' represents the distance from the free surface to the centroid of the wetted area defined by the difference between $A_{j+1/2}(h_j)$ and $A_{j-1/2}(h_j)$. For example, in the case of a trapezoidal channel where the bottom width increases, $b = b(x)$, while the side slope is constant, $m = m_o$, $\bar{y}' = h/2$. On the other hand, when the bottom width is constant, $b = b_o$, while the side slope increases, $m = m(x)$, $\bar{y}' = h/3$. In the more general case where $b = b(x)$ and $m = m(x)$, \bar{y}' will be a linear average of $h/2$ and $h/3$ based on $m(x)$ and $b(x)$. Specifically,

$$\bar{y}' = \frac{\Delta A_m h/2 + \Delta A_b h/3}{\Delta A_m + \Delta A_b} \quad (35)$$

where ΔA_m and ΔA_b are the difference in areas between the right and left face assuming that m and b are held constant, respectively. In the case of natural channels with non-trapezoidal channel cross-section, the calculation of \bar{y}' is more involved, but the same conceptual approach applies.

Corrector Step

In the corrector step of Hancock's scheme, the cell-averaged solution is advanced from the base time level to the next full time level. A semi-implicit approach is again employed to avoid instabilities associated with the friction slope at the wet/dry interface. Consequently, the update equation is given by

$$U_j^{k+1} = U_j^k - \frac{\Delta t}{\Omega} (F_{j+1/2}^{k+1/2} - F_{j-1/2}^{k+1/2}) + \Delta t (S_F)_j^{k+1/2} + \frac{\Delta t}{2} ((S_S)_j^k + (S_S)_j^{k+1}) \quad (36)$$

where

$$S_F = \begin{pmatrix} 0 \\ F_c \end{pmatrix} \quad \text{and} \quad S_S = \begin{pmatrix} 0 \\ gA(S_0 - S_f) \end{pmatrix} \quad (37)$$

Hence, the pressure force F_c and the fluxes F are evaluated explicitly at the half-time level, while the gravity and friction terms are treated implicitly as was done in the predictor step. In this case, the momentum update equation results in a quadratic expression for discharge, Q_j^{k+1} that is solved by the quadratic formula.

Overall, this scheme is stable when the Courant number is less than unity for problems including wave propagation over a dry bed—where fully explicit schemes must resort to very small Courant numbers. In addition, the scheme is second-order accurate in time and space. For mass conservation purposes, it is essential that fluxes be computed globally at an intermediate step between the predictor and the corrector. This leads to mass conservation properties that are consistent with the numerical accuracy, usually $O(10^{-14})$ on computers utilizing double-precision.

Dry Bed Treatment

To manage problems involving wave propagation over an initially dry bed using Hancock's scheme, it is necessary to define a depth ϵ_h , that separates a wetted cell from a dry cell. Here, $\epsilon_h = 10^{-30}$. Then, several checks must be added to the program. First, in the event that a depth less than ϵ_h is computed, the velocity and discharge are set to zero in the cell. Second, in the event that the extrapolated depth at a cell face (h_L or h_R) is less than zero, it should be set to zero prior to applying the numerical flux function. Third, in the event that the depth on both sides of a cell face are less than ϵ_h , the mass and momentum fluxes for the face should be set to zero, and the flux function need not be called. Note: the mass conservation properties are not a function of ϵ_h . That is, ϵ_h can be large and $O(10^{-14})$ mass conservation will still be achieved.

Boundary Conditions

Boundary conditions are implemented by creating ghost cells outside the computational domain where dependent variables and gradients are specified. This then defines a Riemann-type problem at the boundary of the spatial domain that is solved to evaluate the resulting mass and momentum fluxes. Because this approach incorporates the characteristic theory embedded in Roe's flux function, it yields a physically correct solution at the boundary. Recalling that the depth, h , and velocity, V , are extrapolated to cell faces from the cell centers, these are specified in the ghost cell.

At a subcritical inflow boundary where the discharge, Q_o , is specified, the depth is first-order extrapolated using adjacent interior cell values, the area is evaluated from the extrapolated depth, and the velocity is computed as the discharge over the area. In addition, the gradient of the depth is zero-order extrapolated using the adjacent interior cell values, and the gradient in velocity is set to

zero. At a supercritical inflow boundary, both the depth and the velocity are specified in the ghost cell, while the gradients are set to zero.

At an open outflow boundary, both the depth and velocity are first-order extrapolated using adjacent interior cell values, while the gradients are zero-order extrapolated. This treatment simulates a non-reflecting open boundary. If the depth is to be specified at the outflow boundary, the depth in the ghost cell is assigned the specified depth, the velocity is first-order extrapolated, and the gradient in depth and velocity are zero-order extrapolated. To simulate a solid wall, the depth is zero-order extrapolated, the velocity in the ghost cell is set equal and opposite to the velocity in the adjacent interior cell, the gradient in depth the ghost cell is set equal and opposite to the gradient in the interior cell, and the gradient in velocity is zero-order extrapolated.

Interior control structures can also be straightforwardly modeled using the finite volume method. At the location of the control structure, it is sufficient to replace the Riemann solver with a set of equations that evaluate the mass and momentum fluxes through the control structure and any additional forces exerted by the control structure.

Channel junctions should also be treated in the standard way, which is to define a control volume around the junction and to apply an energy conservation equation.

Numerical tests

Prismatic Channels

A series of numerical tests utilizing the well-known dam-break problem are presented to examine the performance of the proposed scheme. First, a triangular channel with $m = 1$ is used. For this case, the exact solution to the dam-break problem is obtained in the standard manner (Henderson 1965), after recognizing that the Riemann invariants are given by $R^+ = V + 4a$ and $R^- = V - 4a$ along $dx/dt = V + a$ and $dx/dt = V - a$, respectively. In this case, there exists wave dispersion that is not captured by the mathematical model. However, it remains appropriate to compare the numerical solution with the exact solution to the mathematical model to measure the scheme's performance.

In this test, the channel is of length $L = 1000m$, it is discretized by $N = 100$ cells, and it is assumed to be horizontal and frictionless. The depth is initially $h = 1.0m$ for $x \leq 500m$ and $h = 0.1m$ otherwise. Time integration is then performed with $Cr_L = 0.25$ where the Courant number Cr_L is defined by,

$$Cr_L = \frac{a_L \Delta t}{\Omega} \quad (38)$$

and the subscript L refers to the stillwater condition to the left, or upstream, of the dam. This corresponds to a Courant number of $Cr = 0.504$ just upstream of the shock. Both Roe's numerical flux function (RFF) and the simplified numerical flux function (SFF) are tested, and the results are presented in Figure 1.

In Figure 1, the Froude number at $t = 112.9 s$ using RFF (line with crosses) and the SFF (line with circles) is presented in addi-

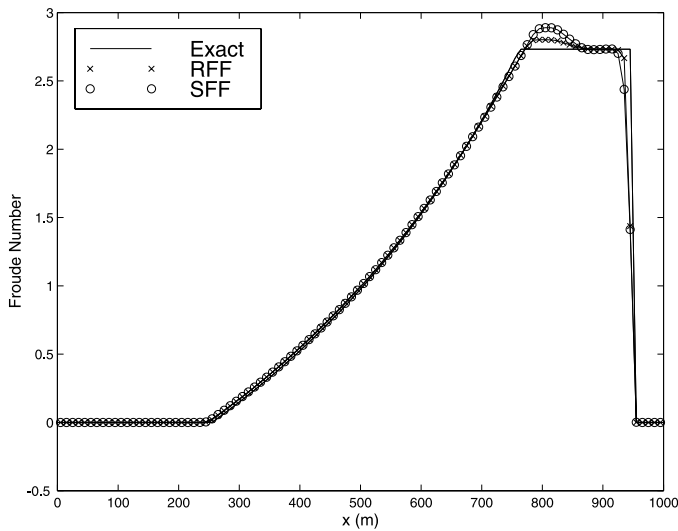


Fig. 1 High resolution dam break problem solution in triangular channel at $t = 112.9s$.

tion to the exact solution (solid line). Noting that the Froude number varies from zero to over 2.5, this represents an example of a transcritical wave problem. The solutions are observed to remain monotone with minimal numerical dissipation. Accuracy is high using both RFF and SFF, though the solution using RFF resolves the supercritical wave action slightly better. This experiment was repeated using smaller and larger values of Cr_L up to the stability limit, and no observable difference in the solution was detected. As was previously discussed, SFF should not be used unless the MUSCL approach, or another approach of variable reconstruction, is also used. To demonstrate the consequences, the previous test is repeated using only a first order time-integration approach, i.e., eliminating the predictor step and evaluating fluxes at the base time level. The time step and cell dimensions are the same as before. The resulting Froude number at $t = 112.9s$ is presented in Figure 2, and the SFF solution can be observed to be considerably poorer than RFF.

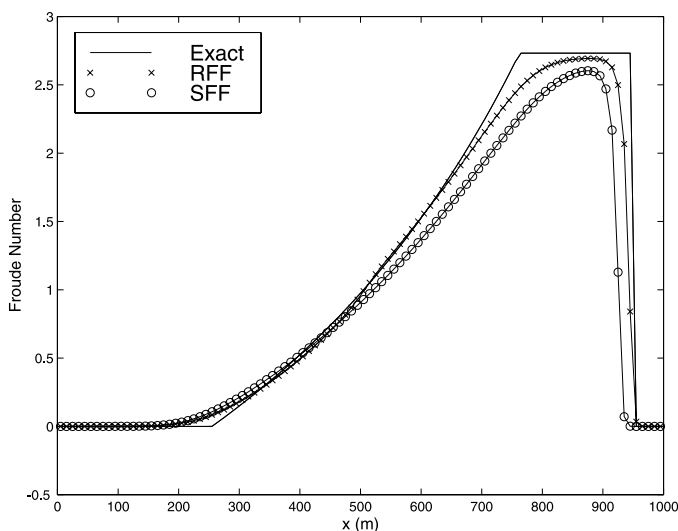


Fig. 2 First order dam break problem solution in triangular channel at $t = 112.9s$.

The performance of the model is next examined by solving the dam-break problem in a trapezoidal channel with $b = 1m$, $m = 2$, and $L = 1000m$. The initial depth is $h = 1.0m$ for $x \leq 500m$ and $h = 0.1m$ otherwise. In Figure 3, the numerical solution at $t = 103.1s$ with $N = 100$, $Cr_L = 0.25$ and using RFF (solid line) and SFF (dashed line) is presented in terms of the Froude number. The solution takes on a familiar shape, is observed to be monotone, and to contain only a minimal amount of numerical dissipation. RFF appears to slightly outperform the SFF in the supercritical flow region.

Next, the dam-break problem is solved in a triangular channel with $m = 1$ using a dry downstream bed. The channel length and spatial discretization remain identical to that used in the previous tests. However, the initial depth for $x > 500m$ is now zero. The solution is obtained using $Cr_L = 0.025$, 0.125 , and 0.25 using RFF. The resulting depth, cross-sectional area, and velocity at $t = 45.16s$ are presented in Figures 4, 5, and 6, respectively.

The dry bed problem represents a challenging numerical problem as a result of the singularity that occurs at the leading edge of the advancing front. In addition, cross-sectional area is proportional to the square of the depth in a triangular channel, so the advancing front is more difficult to resolve here than in the case of a rectangular channel. Nevertheless, Figures 4, 5 and 6 reveal that the solution is well resolved by the model, except at the leading edge of the advancing front. No observable error can be detected in the plot of A in Figure 5, however an error in h can be observed at the leading front as is shown in Figure 4. Due to the depth area relationship ($A = h^2$), the computational precision associated with the prediction in area is greater than that for depth, $O(10^{-14})$ versus $O(10^{-7})$, respectively. Hence, it is not surprising that the area prediction appears superior to the prediction of depth (Figures 4 and 5).

The dependence of the solution on the Courant number Cr_L , is evident in the plot of velocity in Figure 6. The numerical scheme accurately computes the speed of the advancing front using $Cr_L = 0.125$, while larger and smaller values of Cr_L underpredict and overpredict the speed, respectively. Because the Riemann

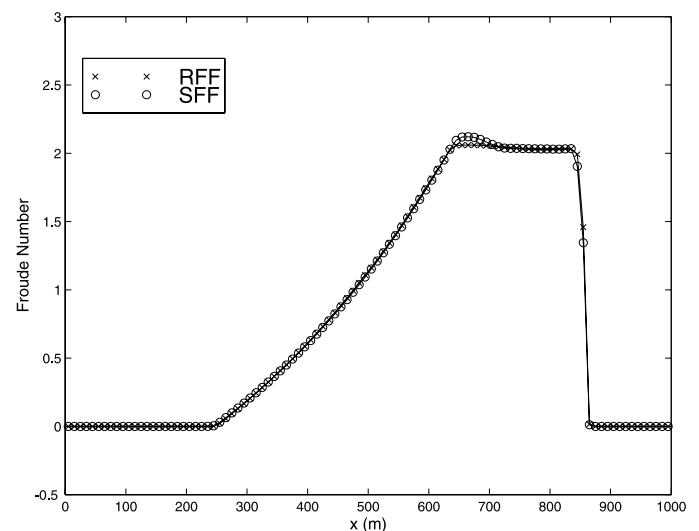


Fig. 3 High resolution dam break problem solution in trapezoidal channel at $t = 103.1s$.

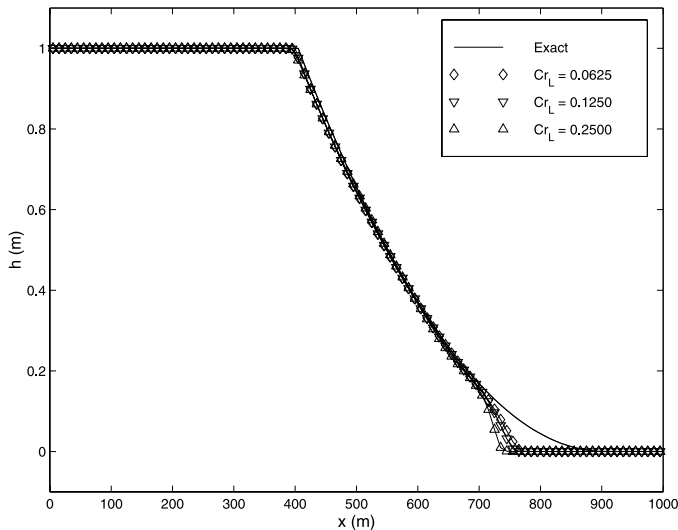
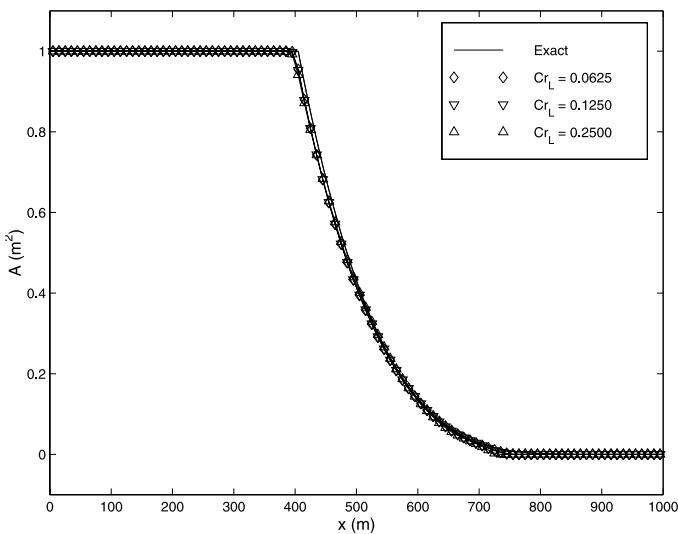


Fig. 4 High resolution dam break problem solution (depth) at $t = 45.16s$ in triangular channel with dry downstream bed.

invariants for this problem are $R^+ = V + 4a$ and $R^- = V - 4a$, the speed of the advancing front is precisely $4a_L$ when $V_L = 0$. Consequently, $Cr_L = 0.125$ corresponds to a Courant number at the front of $Cr_F = 0.5$. For dry-bed computations, this selection of Cr_F has been shown to accurately track the speed of an advancing front on a dry bed using a Roe-type Riemann solver (Bradford 1996, Bradford and Katopodes 1999). From a practical perspective, the overall performance of the scheme is particularly attractive because the solution remains stable, monotone, and highly accurate away from the wet/dry interface without requiring special front-tracking techniques or deforming grids.

Figure 6 demonstrates that the numerical solution under-predicts the peak velocity. At the advancing front, there exists both a discontinuity in the mass flow rate and a vanishing depth. To maintain monotonicity, the scheme adds some dissipation and this acts to smear out the velocity profile. Bradford (1996) reported similar



4Fig. 5 High resolution dam break problem solution (cross-sectional area) at $t = 45.16s$ in triangular channel with dry downstream bed.

results for dry-bed computations using Hancock's scheme and Roe's method in a rectangular channel, so this feature is not unique to the problems considered here.

Non-Prismatic Channels

The scheme is now tested in a non-prismatic channel to evaluate the performance of the proposed treatment of F_c . First, the ability of the scheme to maintain a still-water condition in the presence of a variable cross-sectional geometry is examined. A channel with a length of $L = 1000m$ with $m = 1$ and $b = 1 + 5x/L$ is considered. It is discretized by $N = 100$ cells, a time step of 1 second is used, and the RFF is used. The depth is initially $h = 1m$, and $V = 0$ m/s. The channel boundaries are treated as solid walls. After integrating for 500 time steps to $t = 500s$, there is no measurable difference between the solution at $t = 0s$ and $t = 500s$. That is, momentum and continuity are balanced to the numerical precision of the algorithm, in this case $O(10^{-14})$. This test is repeated for $b = 1m$ and $m = 1+5x/L$, and similarly excellent results are obtained. Hence, the accuracy of the treatment of F_c is found to be consistent with the accuracy of the momentum flux evaluation to $O(10^{-14})$. Similar results are obtained using SFF.

The scheme is next tested on a partial dam-break problem and compared with data collected at the Waterways Experiment Station (WES) of the U.S. Army Corps of Engineers (WES 1960). This problem represents a rigorous test for the proposed scheme due to the multidimensional nature of the wave action and the contraction in channel width at the dam. The experimental setup consists of a 122m long, 1.22m wide rectangular flume with a slope $S_0 = 0.005$, and a removable dam 0.305m high located at the midpoint of the flume. A series of tests were performed at WES, but of interest to this study is an experiment involving a constricted breach with a width of 0.122m, or $1/10^{th}$ of the channel width. The channel bed was smooth for this test and the Manning coefficient was determined to be $n = 0.009$ (WES 1960, Chen 1980). In addition, the flume was initially filled to the height of the dam upstream with a velocity of zero, and the bed was dry

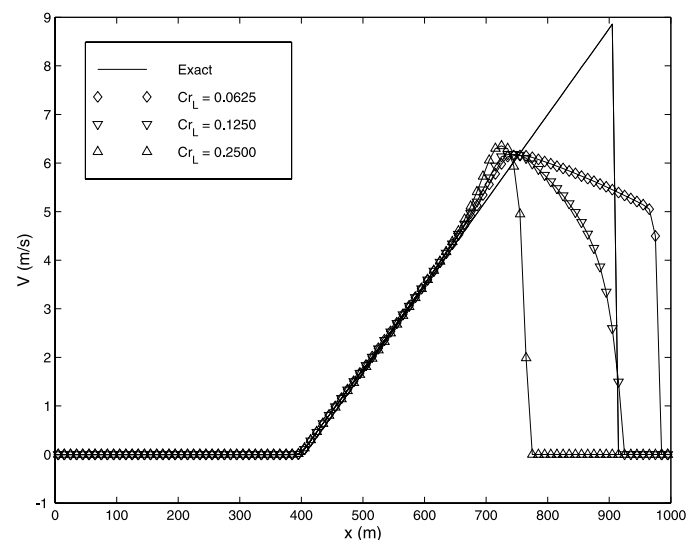


Fig. 6 High resolution dam break problem solution (velocity) at $t = 45.16s$ in triangular channel with dry downstream bed.

downstream. At $t = 0$, the dam was quickly removed with a pulley system.

In the computational model, the channel is discretized by $N = 100$ cells, $Cr_L = 0.125$ (based on the wave speed just upstream of the dam), and RFF is used. In addition, b is specified as the breach width ($0.122m$) at one cell face located at the dam, while it is given as the channel width ($1.22m$) otherwise.

Plots of depth versus time at four measurement stations are present in Figure 7. The measuring stations presented here are STA100 ($x = 30.5m$ measured from the upstream boundary), STA150 ($x = 45.75m$), STA225 ($x = 68.625m$), and STA 350 ($x = 106.75m$). Plots of velocity versus time at STA225 and STA350 are presented in Figure 8. Overall, the agreement between data and model results is excellent.

These results reveal that the scheme accurately resolves the wave action in the flume. First, the timing of the advancing front is accurately depicted as is evident from the depth and velocity hydrographs at STA225 and STA350. The depth at all stations is very well resolved, and the velocity at STA225 is also well resolved. At STA350, the model slightly overestimates the velocity. Nevertheless, the numerical solution remains monotone and mass is again conserved to numerical accuracy.

This test was previously considered by Chen (1980), who solved the St. Venant Equations by the method of characteristics and achieved similar results. However, an ad-hoc approach involving the delineation of a 'conveyance width', a fraction of the total channel width, was required for the portion of the channel upstream of the breach. In addition, 2-3% of the mass was reportedly lost by computational error. In contrast, the scheme presented here is far more robust: there is not a single tuning parameter, mass is conserved to numerical precision, the advancing front is accurately tracked, and the solution remains monotone and accurate.

Conclusions

A high-resolution and monotone solution of the St. Venant equa-

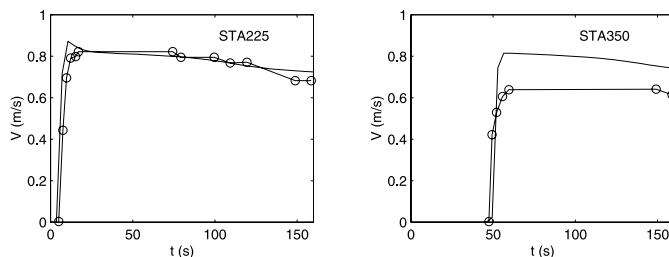


Fig. 8 Model predicted velocity (line) and measured values (line circles) for WES experiment

tions has been achieved for non-rectangular and non-prismatic channels using a MUSCL finite volume scheme with a Roe-type numerical flux function. Hence, this paper demonstrates that the finite volume method yields an open channel flow solver that is applicable well beyond the restricted set of test problems previously considered. Comparisons between model results, exact solutions, and experimental data presented here show that the scheme is accurate and monotone in subcritical, supercritical, and transcritical flow problems, problems involving a dry bed, and problems involving a variable channel cross-sectional shape. In addition, the scheme conserves mass to numerical precision in all simulations including those associated with dry-bed problems. The robust nature of the scheme may make it particularly attractive for engineering practice.

The scheme is founded on the integral form of the mass and momentum conservation equations, and as a result, a treatment is introduced for the pressure force exerted by the channel walls in the flow direction. This treatment is shown to balance the channel wall pressure force with the momentum fluxes to numerical precision, i.e., $O(10^{-14})$. Irregularities in channel cross-section, such as the channel constriction that accompanies bridge abutments, can be discretized using only a single cell interface, i.e., without the need for grid refinement.

Two numerical flux functions are considered for solving the Riemann-type problem found at each cell face: Roe's numerical flux function and a simplified version of Roe's numerical flux function proposed by Nujic (1995). Roe's flux function slightly outperforms the simplified flux function in a series of dam-break problems, but at a modestly greater computational expense. The simplified flux function should only be used only the context of a second-order accurate scheme.

Acknowledgments

Funding for this research was sponsored by a grant from the University of California Water Resources Center (#W 908), whose support is gratefully acknowledged. In addition, the author wishes to express his thanks to Scott F. Bradford of the U.S. Naval Research Laboratory in Washington for helpful comments and discussions related to this work.

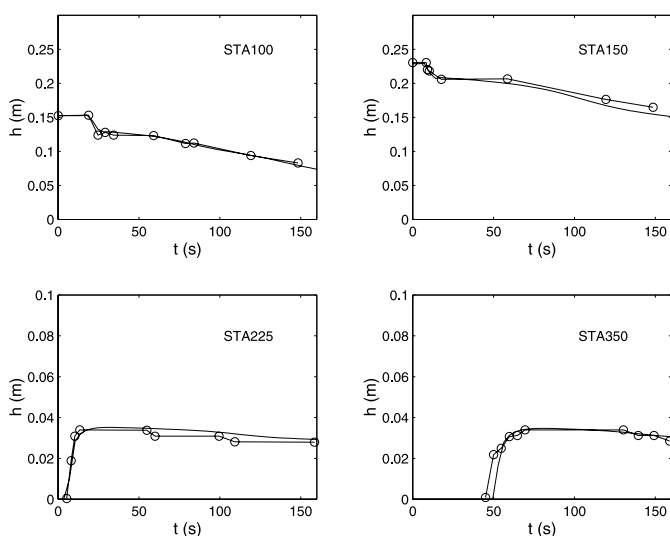


Fig. 7 Model predicted depth (line) and measured values (line circles) for WES experiment

References

- ALCRUDO, F., GARCIA-NAVARRO, P., and SAVIRON, J.-M. (1992) 'Flux-difference Splitting for 1D Open Channel Flow Equations,' *International Journal for Numerical Methods in Fluids*, 14, pp. 1009-1018.
- ALCRUDO, F. and GARCIA-NAVARRO, P. (1993), 'A High-Resolution Godunov-Type Scheme in Finite Volumes for the 2D Shallow-Water Equations,' *International Journal for Numerical Methods in Fluids*, Vol. 16, pp. 489-505.
- BRADFORD, S.F. (1996) Numerical Modeling of Turbidity Current Hydrodynamics and Sedimentation, Ph.D. Dissertation, Department of Civil and Environmental Engineering, University of Michigan.
- BRADFORD, S.F. and KATOPODES, N.D. (1999), 'Hydrodynamics of Turbid Underflows Part I: Formulation and Numerical Analysis,' *Journal of Hydraulic Engineering*, 125(10), pp. 1006-1015.
- CHAUDHRY, M.H. (1993) 'Open-Channel Flow,' Prentice Hall.
- CHEN, C. (1980) 'Laboratory Verification of a Dam-Break Flood Model,' *ASCE Journal of the Hydraulics Division*, 106(HY4), pp. 535-556.
- CUNGE, J.A., HOLLY, F.M. Jr., VERWEY, A. (1980) 'Practical Aspects of Computational River Hydraulics,' Pitman.
- GLAISTER, P. (1988) 'Approximate Riemann Solutions of the Shallow Water Equations,' *Journal of Hydraulic Research*, 26(3), pp. 293-306.
- HENDERSON, F.H. (1966) 'Open Channel Flow,' Macmillan.
- HIRSCH, C. (1990) 'Numerical Computation of Internal and External Flows, Vol. 2' John Wiley & Sons.
- KATOPODES, N.D., (1984) 'A Dissipative Galerkin Scheme for Open-Channel Flow,' *ASCE Journal of Hydraulic Engineering*, 110(4), pp. 450-466.
- MINGHAM, C.G. and CAUSON, D.M. (1998) 'High-Resolution Finite-Volume Method for Shallow-Water Flows,' *ASCE Journal of Hydraulic Engineering*, 124(6), pp. 605-614.
- NUJIĆ, M. (1995) 'Efficient Implementation of Non-oscillatory Schemes for the Computation of Free-Surface Flows,' *Journal of Hydraulic Research*, 33(1), pp. 101-111.
- ROE, P.L. (1981), 'Approximate Riemann Solvers, Parameter Vectors, and Difference Schemes,' *Journal of Computational Physics*, Vol. 43, pp. 357-372.
- SANDERS, B.F. and BRADFORD, S.F. (2001) 'High Resolution, Monotone Solution of the Adjoint Shallow-Water Equations,' *International Journal for Numerical Methods in Fluids*, (to appear).
- SWEBY, P.K. (1984), 'High Resolution Schemes Using Flux Limiters for Hyperbolic Conservation Laws,' *SIAM Journal of Numerical Analysis*, Vol. 21, pp. 995-1011.
- VAN ALBADA, G.D., VAN LEER, B., and ROBERTS, W.W. (1982), 'A Comparative Study of Computational Methods in Cosmic Gas Dynamics,' *Astronomy and Astrophysics*, Vol. 108, pp. 76-84.
- VAN LEER, B. (1979), 'Towards the Ultimate Conservative Difference Scheme. V. A Second Order Sequel to Godunov's Method,' *Journal of Computational Physics*, Vol. 32, pp. 101-136.
- VAN LEER, B., LEE, W.T., and POWELL, K.G., (1989), 'Sonic Point Capturing,' *AIAA 9th Computational Fluid Dynamics Conference*, Buffalo, NY.
- WATERWAYS EXPERIMENT STATION (1960) 'Floods Resulting from Suddenly Breached Dams,' *Miscellaneous Paper No. 2-374*, U.S. Army Corps of Engineers, Report 1, Conditions of Minimum Resistance, Vicksburg, Miss.
- ZHAO, D.H., SHEN, H.W., TABIOS III, G.Q., LAI, J.S., and TAN, W.Y. (1994), 'Finite-Volume Two-Dimensional Unsteady-Flow Model for River Basins,' *Journal of Hydraulic Engineering*, 120, pp. 863-883.
- ZHAO, D.H., SHEN, H.W., LAI, J.S. and TABIOS III, G.Q. (1996) 'Approximate Riemann Solvers in FVM for 2D Hydraulic Shock Wave Modeling,' *ASCE Journal of Hydraulic Engineering*, 122, pp. 692-702.

Notation

a	wave speed
b	channel bottom width
A	cross-sectional area
A_U	Jacobian matrix
F_c	force exerted by channel walls
F	flux vector
g	gravitational constant
h	depth of flow
L	length of solution domain
L	matrix of left eigenvectors
m	inverse slope of channel side-wall
N	number of computational cells
R_h	hydraulic radius
R_m	Riemann variable
R	matrix of right eigenvectors
Q	discharge
S_o	bed slope
S_f	friction slope
S	source term vector
t	time variable
T	channel top width
U	vector of conservative variables
V	cross-sectionally averaged velocity
x	distance along channel
\bar{y}	depth from free surface to centroid of wetted area
z	elevation of the bed
λ	eigenvalue of A_U
Λ	matrix of eigenvalues of A_U
Ω	spatial domain of computational cell